Counterion-dependent microrheological properties of *F*-actin solutions across the isotropic-nematic phase transition

Jun He, Michael Mak, Yifeng Liu, and Jay X. Tang*
Department of Physics, Brown University, Providence, Rhode Island 02912, USA
(Received 13 December 2007; revised manuscript received 13 May 2008; published 16 July 2008)

We studied microrheological properties of *F*-actin across the isotropic-nematic phase transition region by video particle tracking (VPT) and by laser deflection particle tracking (LDPT). Both methods track the motion of thermally driven micron-sized beads, and convert the temporal mean square displacement (MSD) to shear moduli. The two methods give consistent results for the elastic modulus G' and less so for the loss modulus G''. As the nematic order parameter increases with actin concentration, $G'_{\parallel}$ (measured parallel to the nematic director) and $G'_{\perp}$ (perpendicular to the director) grow apart, with $G'_{\perp}$ larger than $G'_{\parallel}$. The moduli scale with actin concentration as $G'_{\parallel} \sim c^{0.54\pm0.13}$ and $G'_{\perp} \sim c^{1.38\pm0.15}$. Furthermore, G' and G'' dependence on $[Mg^{2+}]$ were measured and compared for 1 mg/ml isotropic and 4 mg/ml nematic *F*-actin solutions, respectively. In the isotropic phase, G' increases with $[Mg^{2+}]$ up to 6 mM and then plateaus. In the nematic phase, $G'_{\perp}$ is larger than $G'_{\parallel}$, and both $G'_{\perp}$ and $G'_{\parallel}$ increase with $[Mg^{2+}]$ progressively up to 16 mM, above which *F*-actin form large bundles. In both isotropic and nematic phases, G'' only weakly depends on $[Mg^{2+}]$. In conclusion, particle tracking microrheology reveals rich rheological features of *F*-actin affected by the isotropic-nematic phase transition and by tuning weak electrostatic interactions among the protein filaments.

DOI: 10.1103/PhysRevE.78.011908 PACS number(s): 87.16.Ka, 87.15.−v, 83.85.Cg, 64.70.M−

I. INTRODUCTION

Actin is a major cytoskeletal protein present in almost all eukaryotic cells. It is a dominant component in the cytoskeletal network and plays an essential role in a variety of cell functions, such as motility, shape change, division, and mechanoprotection [1]. Monomeric actin (*G*-actin) polymerizes at physiological salt concentrations (e.g., 50 mM KCl and 2 mM $MgCl_2$) to form long filamentous actin (*F*-actin). *F*-actin has a persistence length of 15–18 μm [2,3] and a diameter of 8 nm [4]. For protein concentration up to a few mg/ml, actin filaments form an entangled isotropic network, covering both semidilute and concentrated regimes. Above a threshold concentration, *F*-actin solution undergoes an isotropic to nematic liquid crystalline phase transition [5–7]. The order parameter of *F*-actin solution in the nematic phase has recently been measured to be about 0.75 [8], which indicates imperfect alignment and possible entanglement of actin filaments despite the nematic ordering. Until now, the rheological properties of *F*-actin in the aligned phase have not been investigated.

Particle tracking microrheology has been extensively used to study the viscoelastic properties of soft materials over the past decade [9–18]. The technique involves tracking thermally driven motion of micron-sized spherical particles embedded in the sample. The widely used methods for position detection include, but are not limited to, video particle tracking (VPT) and laser deflection particle tracking (LDPT). A crucial step of microrheology is to convert temporal mean square displacement (MSD) to complex shear modulus (G^*) in the frequency domain via the generalized Stokes-Einstein relation (GSER), derived by Mason and co-workers [9,10]. Here, $G^*=G'+iG''$, where G' is the storage modulus and G'' is the loss modulus. Microrheology requires only a small volume of test material, typically in microliters. It can also probe local viscoelasticity of an inhomogeneous material, which is not accessible by the traditional bulk rheology measurement. In this paper, we use VPT microrheology to measure G' and G'' in the direction parallel and perpendicular to the nematic director, and characterize anisotropic viscoelasticity of nematic *F*-actin solution, with the network more viscoelastic in the direction perpendicular to the director. To our knowledge, this is the first time that VPT microrheology is applied to the nematic *F*-actin system.

There have been many rheological studies on conventional nematic polymer liquid crystals [19–22]. Among the properties investigated are shear modulus as a function of concentration or temperature, and viscosity as a function of shear rate. However, few previous studies cover the anisotropic behavior of shear modulus in the nematic phase. Recently, a piezo-rheometer technique has been used to measure the complex shear rigidity modulus as a function of frequency and temperature of elastomers and polymers [23–25]. Martinoty *et al.* [25] measured G' of nematic elastomers in two geometries, with shear rate perpendicular and parallel to the nematic director, respectively. This study shows anisotropy of viscoelasticity of nematic elastomers, with $G'_{\perp}$ larger than $G'_{\parallel}$. The lowering of $G'_{\parallel}$ in the nematic phase is attributed to the coupling between the shear and the director. Actually, the complex shear modulus $G^*_{\perp}$ and $G^*_{\parallel}$ for the nematic elastomers can be related to certain components of elastic tensor and viscosity tensor [25,26]. Though the nematic elastomer with covalent crosslinks is different from the nematic *F*-actin network without crosslinks, these two systems do have similarly anisotropic viscoelasticity.

Actin filaments are negatively charged polyelectrolytes. When the filaments are parallelly aligned and close to each other, multivalent counterions, such as Mg^{2+}, condensed around them can produce an effective attraction between

*Jay_Tang@Brown.edu

each pair of filaments [27–29]. Such an attractive interaction can induce bundle formation when the counterion concentration reaches a threshold value [30,31]. This attractive interaction may still exist below the threshold concentration, especially in the nematic phase, though it is not strong enough to suppress the thermal fluctuations and keep the filaments bundled. Consistent with this physical conjecture, we recently reported an anomalous slowdown of *F*-actin diffusion in the nematic phase caused by the temporary associations between neighboring filaments facilitated by divalent counterions [32]. Rheological studies on crosslinked actin networks reveal that a very low density of crosslinkers can increase elastic moduli by orders of magnitude [33,34]. Since these counterion induced temporary associations may act similar to weak crosslinkers, we may ask the following questions. Is the viscoelasticity of *F*-actin solution affected by the divalent counterions? If so, is it affected differently in the isotropic and nematic phases? We do find a marked influence of divalent counterions on viscoelastic properties in both phases. These findings provide us important insight in how the viscoelastic properties of biopolymeric materials are affected by the polymer alignment, as well as counterion-mediated interactions between the aligned biopolymers.

II. MATERIALS AND METHODS

A. Sample preparation

Actin was extracted from rabbit skeletal muscle following the technique of Pardee and Spudich [35]. The extracted actin, kept in *G*-buffer (2 mM Tris-HCl, pH 8.0, 0.5 mM ATP, 0.2 mM $CaCl_2$, 0.5 mM DTT, and 0.005% NaN_3) and concentrated to about 7 mg/ml, was frozen with liquid nitrogen and stored at −80 °C. For experiments, aliquots of actin was thawed rapidly on a heatblock to 25 °C and centrifuged for 5 min at 7000 g. The *G*-actin was polymerized to form *F*-actin by adding the salts KCl and $MgCl_2$ to the final concentrations of 50 mM and 2 mM, respectively. For the batch used in the experiments, the average filament length of *F*-actin was detected to be approximately 7 μm under the specified polymerization condition.

We used carboxylate-modified polystyrene beads with diameters of 1, 2, and 3.6 μm (The exact diameters are specified as 0.984, 2.02, and 3.56 μm by the vendor: Polysciences Inc., Warrington, PA). Bead suspensions were diluted with the same ionic solution as that of *F*-actin before they were added to *F*-actin solutions in order to enable proper observation of beads motion without altering the ionic condition of *F*-actin. The mixed solutions were injected into rectangular capillary tubes (VitroCom Inc., Mt. Lakes, NJ) with cross-sectional dimensions of 0.1×1 mm^2. Each capillary was immediately sealed with an inert glue to eliminate flow and evaporation from the system. The direction parallel to the tube long axis is defined as the parallel direction ($\parallel$), and the direction perpendicular to the long axis and in the plane of observation is defined as the perpendicular direction ($\perp$). Due to the shear alignment when the sample was filled, the nematic director typically pointed along the capillary axis. All samples were stored in 4 °C overnight to reach equilibrium, and then brought to room temperature for at least two hours before measurements.

B. Polarization microscopy of nematic director field

The birefringence of nematic actin solution was measured using a polarizing microscope equipped with a liquid crystal universal compensator (LC-PolScope, Cambridge Research and Instrumentation, Woburn, MA). The polarizing microscope, a Nikon Eclipse 800, was operated as described in the literature [36,37]. The LC-PolScope software was used for instrument control, image capture, and computation of retardance and orientation maps. The LC-PolScope system is capable of measuring the optical retardance and orientation of the slow axis at each pixel position, thus reporting local values of retardance and alignment of actin filaments.

C. Video particle tracking microrheology (VPT)

To implement the video particle tracking (VPT) method, we first track the motion of beads imbedded in the material of interest by using a Nikon E800 upright microscope equipped with a Cool-Snap HQ charge-coupled device (CCD) camera (Photometrics, Tucson, AZ). Time-lapse movies of beads were taken in the middle of the capillary cavity using a 100× objective so that the beads were well away from the glass walls or any air-liquid interface. The positions of centroids of beads were obtained by using the thresholding tracking algorithm in Metamorph 6.0 (Universal Imaging Corp., Downingtown, PA).

We then calculate the temporal MSD $\langle \Delta r^2(t) \rangle$ from the bead positions. The modulus $\tilde{G}(s)$ is related to the unilateral Laplace transform of $\langle \Delta r^2(t) \rangle$ through the generalized Stokes-Einstein relation (GSER) [9,10],

$$\tilde{G}(s) = \frac{k_B T}{\pi a s \langle \Delta \tilde{r}^2(s) \rangle}, \tag{1}$$

where s is the Laplace frequency, k_B is the Boltzmann constant, T is the absolute temperature, and a is the bead radius. This equation has been derived by Mason *et al.* (1997), assuming a sphere with negligible mass embedded in an incompressible and isotropically viscoelastic medium with the nonslip boundary condition. The GSER also has a corresponding form in the Fourier domain,

$$G^*(\omega) = \frac{k_B T}{\pi a i \omega \mathcal{F}\{\langle \Delta r^2(t) \rangle\}}. \tag{2}$$

Since the data of $\langle \Delta r^2(t) \rangle$ are in discrete times and over a limited range, implementing a numerical Laplace transform introduces significant truncation errors near the frequency extremes, whereas it does give accurate results well within the region between the two extremes. Similar errors near the frequency extremes may also occur when the fast Fourier transform is used. To overcome the errors, Mason *et al.* [15] estimated the transforms algebraically by applying a local power law expansion around a frequency of interest ω, and retaining the leading term, $\langle \Delta r^2(t) \rangle = \langle \Delta r^2(1/\omega) \rangle (\omega t)^{\alpha(\omega)}$. The evaluation of the Fourier transform can be given as

$$i\omega\mathcal{F}(\langle\Delta r^2(t)\rangle) = \langle\Delta r^2(1/\omega)\rangle[\Gamma(1+\alpha(\omega))]i^{-\alpha(\omega)}, \quad (3)$$

where α is defined as $\alpha(\omega) \equiv \frac{d\ln\langle\Delta r^2(t)\rangle}{d\ln t}|_{t=1/\omega}$. Substituting Eq. (3) into Eq. (2) leads to

$$G'(\omega) = |G^*(\omega)|\cos[\pi\alpha(\omega)/2], \quad (4)$$

$$G''(\omega) = |G^*(\omega)|\sin[\pi\alpha(\omega)/2], \quad (5)$$

where $G'(\omega)$ is the storage modulus and $G''(\omega)$ is the loss modulus, and $|G^*(\omega)| = k_BT/\{\pi a\langle\Delta r^2(1/\omega)\rangle[\Gamma(1+\alpha(\omega))]\}$. Equation (4) and Eq. (5) yield a helpful physical interpretation of moduli in terms of MSD. For a viscous medium, diffusion dominates and α approaches one; G'' becomes prominent and G' vanishes. For a more elastic medium, the motion is more confined and α approaches zero; G' dominates and G'' diminishes.

In this paper, we focus on the rheological properties of *F*-actin in the nematic phase. Assuming that the motion of test spheres in the direction parallel to the nematic director is only determined by $G^*_\parallel(\omega)$ and the motion in the perpendicular direction by $G^*_\perp(\omega)$, we extend the analytical treatment summarized above to an anisotropic medium to obtain $G'_\parallel(\omega)$, $G''_\parallel(\omega)$, $G'_\perp(\omega)$, and $G''_\perp(\omega)$ from two independent one-dimensional (1D) diffusions. Note that Eq. (2) needs to be modified to $G^*_\parallel(\omega) = \frac{k_BT}{2\pi ai\omega\mathcal{F}(\langle\Delta r^2_\parallel(t)\rangle)}$ and $G^*_\perp(\omega) = \frac{k_BT}{2\pi ai\omega\mathcal{F}(\langle\Delta r^2_\perp(t)\rangle)}$, respectively, where the factor of 1/2 arises from the fact that the MSD is now 1D for either direction instead of 2D.

D. Laser deflection particle tracking microrheology (LDPT)

For the LDPT method, we use a Nikon Eclipse TE 2000-U inverted microscope. Laser trap is produced by focusing a laser beam generated by a diode pumped Nd:yttrium-aluminum-garnet (YAG) laser source at 1064 nm infrared wavelength (CrystaLaser LC, Reno, NV). The positions of beads are obtained by detecting the position of the laser spot cast on a quadrant photodetector (custom made by Mr. Winfield Hill, Roland Institute, Cambridge, MA). Voltage outputs for two perpendicular directions are acquired by a BNC 2090 board and processed by LabVIEW (National Instruments, Austin, TX). The experimental setup is the same as described previously in Ref. [17]. The laser power is tuned down by orders of magnitude compared with that required to produce a laser trap, but it is still intense enough for accurate position detection.

To convert the positions of beads to moduli, we follow the procedure described by Schnurr *et al.* [11] and Gittes *et al.* [12], using the generalized Stokes relation (GSR). When a force is applied on a sphere, the linear response for the sphere can be calculated from the deformation of the surrounding medium, $r_\omega = \alpha(\omega)f_\omega$, where r is the position of the sphere. Generally, the response function has a complex form $\alpha^*(\omega) = \alpha'(\omega) + i\alpha''(\omega)$. This response function is related to the complex shear modulus by the GSR

$$\alpha^*(\omega) = \frac{1}{6\pi G^*(\omega)a}. \quad (6)$$

This equation has been derived and justified in Ref. [11]. The imaginary part of the response function $\alpha''(\omega)$ can be related to the power spectral density (PSD) of 1D thermal motion $\langle r^2_{\parallel,\perp}(\omega)\rangle$ (Fourier transform of MSD) of either parallel or perpendicular direction by the fluctuation-dissipation theorem [38] as

$$\alpha''(\omega) = \frac{\omega}{2k_BT}\langle r^2_{\parallel,\perp}(\omega)\rangle. \quad (7)$$

The real part $\alpha'(\omega)$ is obtained from the imaginary part $\alpha''(\omega)$ via the Kramers-Kronig relation [38] by evaluating the dispersion integral

$$\alpha'(\omega) = \frac{2}{\pi}P\int_0^\infty d\zeta\frac{\zeta\alpha''(\omega)}{\zeta^2-\omega^2} = \frac{2}{\pi}\int_0^\infty dt\cos\omega t\int_0^\infty d\zeta\alpha''(\zeta)\sin(\zeta t), \quad (8)$$

where P indicates the principal-value integral. Finally, $G^*(\omega)$ is obtained from the reciprocal of $\alpha^*(\omega)$,

$$G'(\omega) = \frac{\alpha'(\omega)}{6\pi a[\alpha'^2(\omega)+\alpha''^2(\omega)]}, \quad (9)$$

$$G''(\omega) = \frac{-\alpha''(\omega)}{6\pi a[\alpha'^2(\omega)+\alpha''^2(\omega)]}. \quad (10)$$

For a nematic solution, the response function in the parallel and perpendicular directions $\alpha^*_\parallel$ and $\alpha^*_\perp$ are different. Assuming decoupling of the motion in the two directions, we consider separate response functions, $r_\parallel(\omega) = \alpha^*_\parallel(\omega)f_\parallel(\omega)$ and $r_\perp(\omega) = \alpha^*_\perp(\omega)f_\perp(\omega)$. Using Eqs. (7)–(10), we obtain accordingly $G'_\parallel(\omega)$, $G''_\parallel(\omega)$, $G'_\perp(\omega)$, and $G''_\perp(\omega)$.

The VPT and the LDPT methods each have their own advantages and limitations. The VPT method can track multiple particles at the same time and is convenient to implement, yet it is not capable of giving high frequency information due to the limited resolution and response time of the CCD camera. Additionally, since the amount of memory available to take the video is limited, the VPT method cannot take more than a few thousand frames. Consequently, the direct Fourier transform introduces a significant truncation error across the whole frequency range, so the power expansion method is more suitable for the VPT method. On the other hand, the laser has much faster response time to changes over the bead position in order to obtain the high frequency spectrum. The LDPT method readily acquires data of 10^6 positions, which can be efficiently processed by the direct Fourier transform but not by the power expansion method. This is because it takes a long time for the power expansion method to compute the slope and moduli at each point. Because of the large amount of data, leaving out the regions at both low and high frequency extremes with large truncation errors still yields accurate results in a wide enough range. The disadvantage of the LDPT method is that the

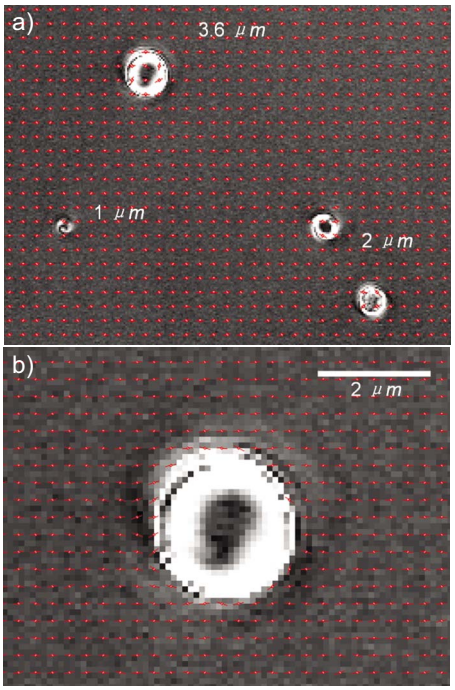

FIG. 1. (Color online) Birefringence image of nematic actin solution with beads embedded. The sample is measured between a glass slide and a cover slip. The average sample thickness is 12 ± 2 μm, and the average retardance is about 0.99 nm. (a) A region with beads of three diameters 1 μm, 2 μm, and 3.6 μm is shown. The red pins indicate the local orientations of the filaments. The length of each red pin is 0.5 μm, serving as a convenient scale bar. The distortion within the projected areas of beads is due to the birefringence of beads themselves. (b) A zoomed-in image with one 3.6 μm bead at the center is shown. The red pins indicate the local orientations of the filaments.

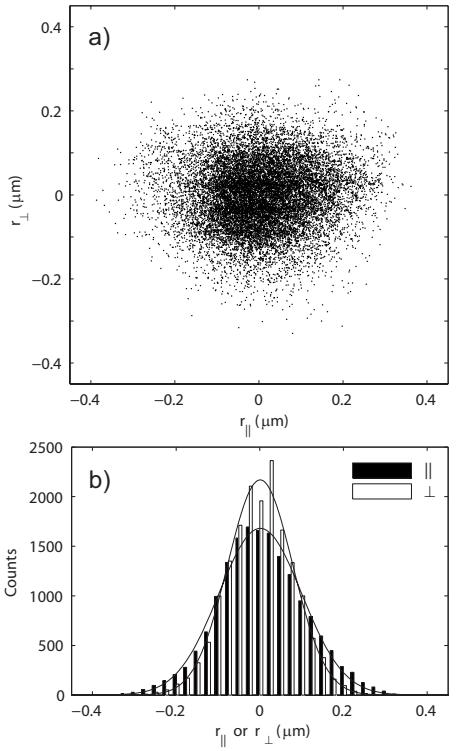

FIG. 2. (a) The overlap of positions of 1 μm beads over time in a 1 mg/ml isotropic *F*-actin solution. Each dot stands for the centroid of a bead in a particular frame, and the graph is a collection of ten beads with 2000 frames per bead taken at the rate of 10 frames/sec. (b) The histograms showing the distributions of bead positions in the parallel (dark bar) and perpendicular (gray bar) directions. The solid lines are Gaussian fits for the distributions. The standard deviations from the fits for the data in parallel and perpendicular directions are 0.14 μm and 0.11 μm, respectively.

focused laser beam applies a trapping force on the tracer bead and alters its free motion; it requires a calibration of the conversion factor from voltage to displacement every time and needs to have the trap stiffness subtracted from G'. For measuring the dependence of moduli on actin concentration and ion condition, we are mostly interested in the low frequency range, where the VPT method yields reliable results. Therefore, we use primarily the VPT method for the measurements of shear moduli. LDPT, as a complementary approach, is performed under selected conditions to show the high frequency behavior.

III. RESULTS

A. Effects of probe beads on nematic ordering

Inclusion of spherical particles in nematic liquid crystals could induce defects [39–41]. In order to assess for possible distortions and defects of nematic actin network due to the inclusion of spherical particles, we performed birefringence imaging using a PolScope retardance imaging system. The birefringence of nematic actin solution with beads embedded are shown in Fig. 1. The sample is measured between glass slide and cover slip sealed with vacuum grease. The average thickness is about 12 ± 2 μm, and the average retardance is about 0.99 nm. Figure 1(a) shows a larger field of view with test beads of 1 μm, 2 μm, and 3.6 μm in diameter. The general alignment is along the horizontal direction, and is not affected significantly by the beads. Figure 1(b) shows a zoomed-in image around the 3.6 μm bead, which is expected to produce the largest distortion among the three sizes. The distortion of the network is localized over a thin layer around the bead and decays within a micron or two from the bead surface. Also, no defect is observed across the whole sample. Thus, the nematic *F*-actin network is not severely distorted by micron-sized beads. This conclusion validates our approach to use beads as a probe to study the microrheological properties of nematic *F*-actin networks.

B. Anisotropic bead diffusion in the nematic phase

The positions of beads at different times were extracted from a time-lapse movie recorded by phase contrast microscopy. Figure 2(a) shows a collection of positions of ten 1 μm beads in a 1 mg/ml isotropic *F*-actin solution, with 2000 frames per bead taken at the frame rate of 10 frames/sec. The distribution of the bead positions are roughly rotationally symmetric. Figure 2(b) shows the position distributions of beads in the parallel and perpendicular directions. The

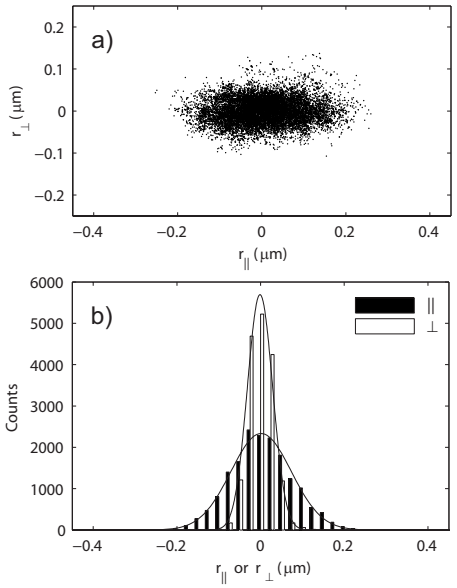

FIG. 3. (a) The overlap of positions of 1 μm beads over time in a 4 mg/ml nematic *F*-actin solution. It is an overlap of trajectories of ten beads with 2000 frames per bead taken at the rate of 10 frames/sec. (b) The histograms showing the distributions of beads in the parallel (dark bar) and perpendicular (gray bar) directions. The solid lines are Gaussian fits for the distributions. The distribution in the perpendicular direction is narrower than that in the parallel direction. The standard deviation from the fit for the parallel direction is about 0.086 μm, and for the perpendicular direction it is about 0.036 μm.

distributions in both directions are Gaussian and the widths of the distributions in the two directions are about the same, confirming isotropic diffusion of beads in the isotropic solution. The slightly larger standard deviation in the parallel direction than perpendicular direction is likely due to residual alignment along the capillary axis when the polymerizing *F*-actin is filled into the long capillary. Figure 3(a) shows a similar collection of positions of ten beads in a 4 mg/ml nematic *F*-actin solution, and Fig. 3(b) gives the position distributions of beads in the parallel and perpendicular directions. In the nematic solution, the distributions of bead positions in the two directions are also both Gaussian, but the beads diffuse preferentially along the parallel direction (the nematic director). The standard deviation of the distribution in the parallel direction is about 0.086 μm, and in the perpendicular direction it is about 0.036 μm. Hence, the width of the distribution in the parallel direction is more than twice that in the perpendicular direction. From the distributions of bead positions, we see that the bead diffusion in the isotropic solutions is symmetric in all directions, but the bead diffusion in the nematic solution is anisotropic, showing more motion along the direction of alignment.

C. Mean square displacement

The mean square displacements (MSDs) of beads for different time intervals have been calculated from the coordinates obtained from the VPT method. Figure 4 shows typical MSDs of 1 μm beads in log-log plots for a 1 mg/ml isotropic solution and a 4 mg/ml nematic solution. For the 1 mg/ml isotropic solution, the MSDs in the parallel (■) and perpendicular directions (□) are about the same, showing isotropic diffusion. For the 4 mg/ml nematic solution, the bead diffusion is anisotropic. The MSD is larger in the parallel direction (▲) than in the perpendicular direction (△) showing preferable diffusion along the nematic director.

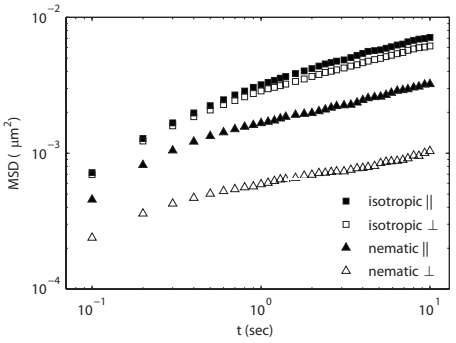

FIG. 4. Mean square displacement (MSD) of 1 μm beads as a function of time interval for 1 mg/ml isotropic solutions and 4 mg/ml nematic solutions. MSDs in the isotropic phase are shown in squares, and MSDs in the nematic phase in triangles. MSDs parallel to the tube long axis are shown in solid symbols, and those perpendiculer to the tube long axis are shown in open symbols. $[Mg^{2+}]$ in either sample is 2 mM.

D. Frequency spectrum of shear moduli of nematic *F*-actin solutions

Frequency dependence of shear moduli can be obtained from the MSD via the GSER by implementing the power expansion method [Eqs. (2)–(5)]. In Fig. 5, G' and G'' of parallel and perpendicular directions are plotted against frequency for the 1 mg/ml isotropic *F*-actin solution containing 2 mM Mg^{2+}. For the isotropic phase, $G'_{\|}$ and $G'_{\perp}$ differ very little, and the same holds for $G''_{\|}$ and $G''_{\perp}$, showing isotropic viscoelasticity. The small difference between the moduli of two directions could be due to the weak metastable filament alignment in the 1 mg/ml sample caused by the shear flow

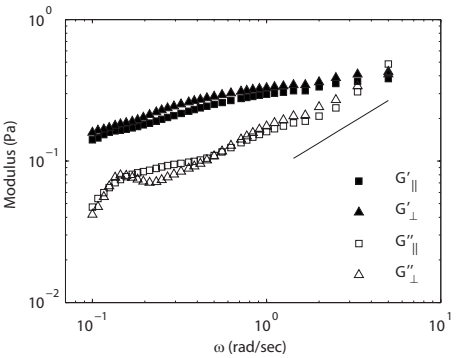

FIG. 5. Frequency dependence of G' (solid symbols) and G'' (open symbols) measured by the video particle tracking (VPT) method for 1 mg/ml isotropic *F*-actin solution in the parallel (squares) and perpendicular direction (triangles). The spectrum is obtained by averaging over measurements of ten beads.

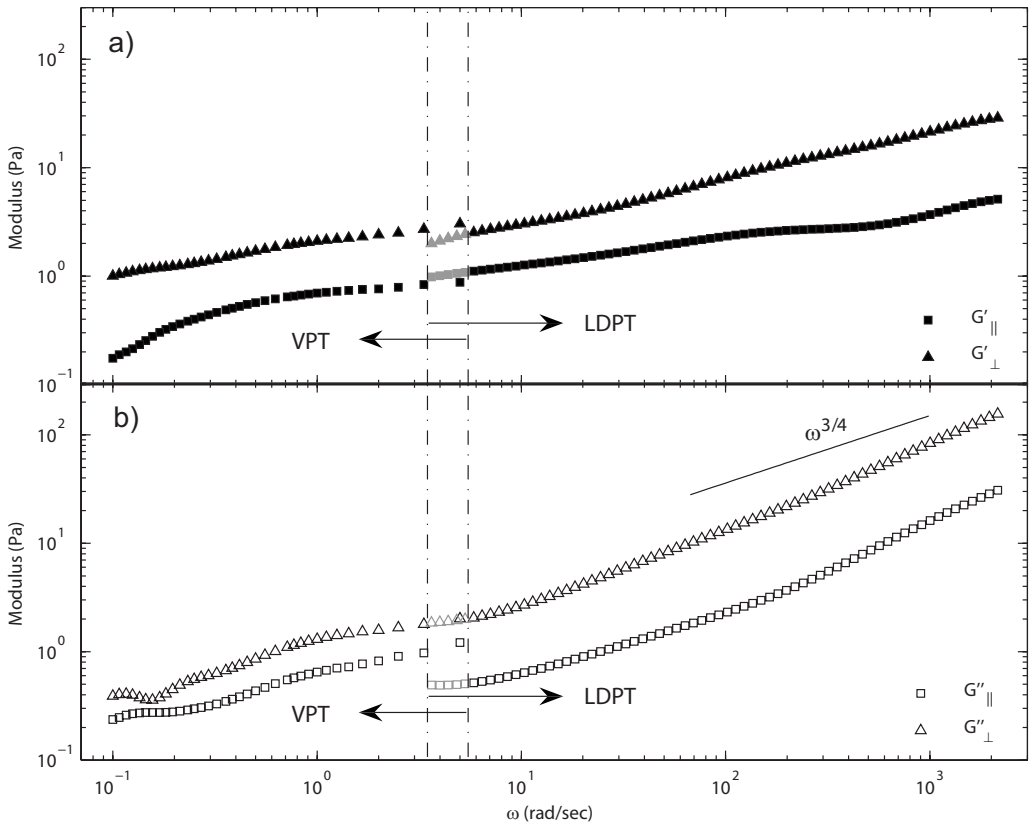

FIG. 6. Frequency dependence of moduli for a 4 mg/ml nematic *F*-actin solution. (a) The spectra of $G'_{\parallel}$ and $G'_{\perp}$ in solid symbols; (b) spectra of $G''_{\parallel}$ and $G''_{\perp}$ in open symbols. For the spectra on the left, the bead position tracking was performed with the VPT method and the MSD was converted to moduli with GSER by implementing the power expansion method; for the spectrum on the right, the bead positions were tracked by the LDPT method with the position data converted to moduli via GSR by implementing fast Fourier transform of MSD. In the overlap region between the two dash dot lines, the LDPT results are shown in gray symbols. The two methods give consistent results for $G'_{\parallel}$, $G'_{\perp}$, and $G''_{\perp}$; $G''_{\parallel}$ measured by the VPT method, however, is about twice of that measured by LDPT. Both the VPT and LDPT spectra were measured using 1 μm beads and obtained from averaging over ten beads. The solid straight line shows a scaling law of $\omega^{3/4}$.

as the sample was filled into the capillary. The G's have a weak dependence on frequency, showing the characteristic of a plateau modulus. The values of G' obtained are very close to those measured by Gardel *et al.*, between 0.2 and 0.3 Pa for 1 mg/ml *F*-actin [42]. The G''s increase with frequency approximately in a scaling relation of $G'' \sim \omega^{3/4}$, consistent with the microrheology measurements by Gittes *et al.* [12], Xu *et al.* [14], and Mason *et al.* [43], and also with the recent optical tweezers passive microrheology results by Brau *et al.* [18]. The VPT microrheology measurements by Gardel *et al.* [42], however, gave a scaling relation of $G'' \sim \omega^{1/2}$ for a 1 mg/ml *F*-actin solution using 0.84 μm diameter beads. The extra bump and dip in the low frequency range of G'' spectra are likely artificial, due to smoothing of the noisy data.

For the 4 mg/ml nematic *F*-actin solution containing 2 mM Mg^{2+}, frequency spectra of G' and G'' of parallel and perpendicular directions are shown in Fig. 6. For the low frequency data on the left, the bead tracking was done with the VPT method and the MSD data were processed with the power expansion method. For the high frequency data on the right, the bead positions were tracked with the LDPT method and the MSD data were converted to the shear moduli via the GSR by directly implementing the fast Fourier transform of the MSDs. For the LDPT method, the trap stiffness is subtracted from G's; data of frequencies about 1/2 decade at the lower and higher ends with large truncation errors have been deleted. The moduli measured by the LDPT method are shown in gray symbols in the overlap region. For this particular sample, $G'_{\parallel}$, $G'_{\perp}$, and $G''_{\perp}$ measured by the two methods agree, evident by the consistent values in the overlap region; $G''_{\parallel}$ measured by VPT is about twice that measured by LDPT in the overlap region. $G'_{\parallel}$ and $G'_{\perp}$ both show the behavior of plateau modulus. $G''_{\parallel}$ and $G''_{\perp}$ follow a scaling behavior of $\omega^{3/4}$, the same as in the isotropic phase. $G'_{\perp}$ and $G''_{\perp}$ are larger than $G'_{\parallel}$ and $G''_{\parallel}$, respectively, across the entire frequency range measured by the two methods. $G'_{\perp}$ is about three times $G'_{\parallel}$. $G''_{\perp}$ is either about twice $G''_{\parallel}$ as measured by the VPT method, or four times $G''_{\parallel}$ as measured by the LDPT method.

In summary, the viscoelastic properties are isotropic for isotropic *F*-actin solutions, whereas the nematic *F*-actin solution is more viscoelastic in a direction perpendicular to the nematic director. The VPT and the LDPT methods give consistent results for the frequency spectra of shear moduli with the exception of $G''_{\parallel}$. The cause of such discrepancy is unknown and merits further investigation.

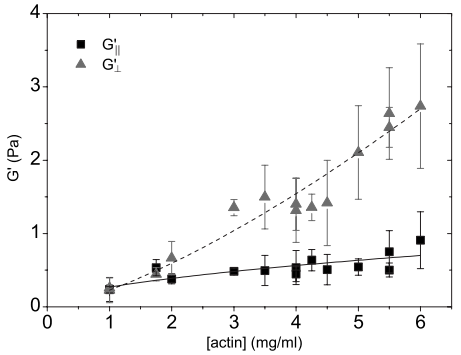

FIG. 7. $G'_{\parallel}$ (solid squares) and $G'_{\perp}$ (gray triangles) at 0.3 rad/sec are plotted against actin concentration across *I-N* phase transition of *F*-actin solution, measured by the VPT method using 1 μm beads. The onset concentration of *I-N* transition is about 2 mg/ml. The solid line is a power law fit to $G'_{\parallel}$, yielding a scaling exponent of 0.54 ± 0.13; the dashed line is a power law fit to $G'_{\perp}$, yielding a scaling exponent of 1.38 ± 0.15.

E. Shear modulus versus actin concentration across the isotropic-nematic phase transition

In order to investigate the effect of *I-N* transition on the rheological properties of *F*-actin, we have measured $G'_{\parallel}$ and $G'_{\perp}$ as a function of actin concentration from 1 mg/ml to 6 mg/ml (Fig. 7). The values are taken at 0.3 rad/sec from the frequency spectrum for a convenient comparison. The average length of actin filaments is measured to be about 7 μm. The onset concentration for the nematic phase transition is around 2 mg/ml. $G'_{\parallel}$ and $G'_{\perp}$ start at about the same value for the 1 mg/ml isotropic solution. As the actin concentration increases and the system enters the nematic phase, $G'_{\parallel}$ and $G'_{\perp}$ grow apart, with $G'_{\perp}$ larger and increasing more steeply than $G'_{\parallel}$. The ratio of $G'_{\perp}$ to $G'_{\parallel}$ grows from 1 to 4, as the actin concentration increases from 1 mg/ml to 6 mg/ml. We find that $G'_{\perp}$ scales with actin concentration as $G'_{\perp} \sim c^{1.38 \pm 0.15}$, whereas $G'_{\parallel}$ has a weaker dependence on actin concentration and scales as $G'_{\parallel} \sim c^{0.54 \pm 0.13}$. The scaling behavior of $G'_{\perp}$ is similar to the bulk rheology results in the isotropic phase $G' \sim c^{1.4}$ [44]. The scaling of $G'_{\parallel}$ with actin concentration in the nematic phase yields a smaller power exponent than that of $G'_{\perp}$. This feature is further discussed in Sec. IV.

F. Dependence of shear moduli on the Mg^{2+} concentration in isotropic and nematic phases

From our previous study of *F*-actin diffusion across the isotropic-nematic phase transition, we found that *F*-actin diffusion is affected by $[Mg^{2+}]$ more in the nematic phase than in the isotropic phase [32]. It is therefore expected that $[Mg^{2+}]$ may alter the rheological properties of *F*-actin solution more in the nematic phase than in the isotropic phase. We measured for comparison $G'_{\parallel}$, $G'_{\perp}$, $G''_{\parallel}$, and $G''_{\perp}$ as a function of $[Mg^{2+}]$ for 1 mg/ml isotropic and 4 mg/ml nematic *F*-actin solutions (Fig. 8). In Fig. 8(a) for the isotropic solutions, $G'_{\parallel}$ (◆) and $G'_{\perp}$ (▼) are very close for all $[Mg^{2+}]$, and the same holds true for $G''_{\parallel}$ (◇) and $G''_{\perp}$ (▽), showing isotropic viscoelastic properties. In either direction, the G's increase with $[Mg^{2+}]$ up to 6 mM and then plateaus, and the G''s are less sensitive to $[Mg^{2+}]$. In Fig. 8(b) for the nematic solutions, $G'_{\perp}$ (▲) is larger than $G'_{\parallel}$ (■) for all $[Mg^{2+}]$, and they both increase with $[Mg^{2+}]$ in a larger range up to 16 mM, above which *F*-actin forms large bundles and the sample becomes highly inhomogeneous. The G''s are less sensitive to $[Mg^{2+}]$, especially $G''_{\perp}$. $G''_{\perp}$ (△) varies little with $[Mg^{2+}]$ until the threshold of bundle formation is approached, starting larger than $G''_{\parallel}$ (□) but becoming smaller than $G''_{\parallel}$ at $[Mg^{2+}]$ of a few mM. On the whole, the moduli of *F*-actin solutions are more affected by $[Mg^{2+}]$ in the nematic phase than in the isotropic phase.

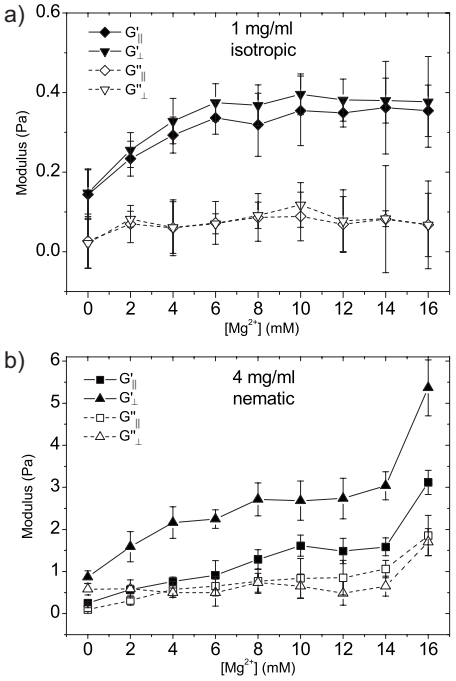

FIG. 8. G' and G'' in the parallel and perpendicular directions as a function of $[Mg^{2+}]$ measured by the VPT method at 0.3 rad/sec using 1 μm beads. (a) For the 1 mg/ml isotropic solution, $G'_{\parallel}$ is in ◆, $G'_{\perp}$ in ▼, $G''_{\parallel}$ in ◇, and $G''_{\perp}$ in ▽; (b) for the 4 mg/ml nematic solution, $G'_{\parallel}$ is in ■, $G'_{\perp}$ in ▲, $G''_{\parallel}$ in □, and $G''_{\perp}$ in △.

IV. DISCUSSION

A. Anisotropy of viscoelastic properties of nematic *F*-actin networks

Based on the measured MSD, distinct rheological properties are shown between isotropic and nematic actin solutions. For isotropic *F*-actin solutions, the storage modulus (G') and loss modulus (G'') are about the same in the directions parallel and perpendicular to the tube long axis across the whole frequency range (Fig. 5). The nematic *F*-actin solutions, however, display anisotropic viscoelasticity, with higher moduli in the direction perpendicular to the alignment of filaments. As shown in Fig. 6, $G'_{\perp}$ and $G''_{\perp}$ are larger than $G'_{\parallel}$ and $G''_{\parallel}$, respectively, over the entire frequency range.

The anisotropic bead diffusion and viscoelasticity of nematic *F*-actin solutions can be interpreted based on the tube model [45,46], which describes the motion of an individual

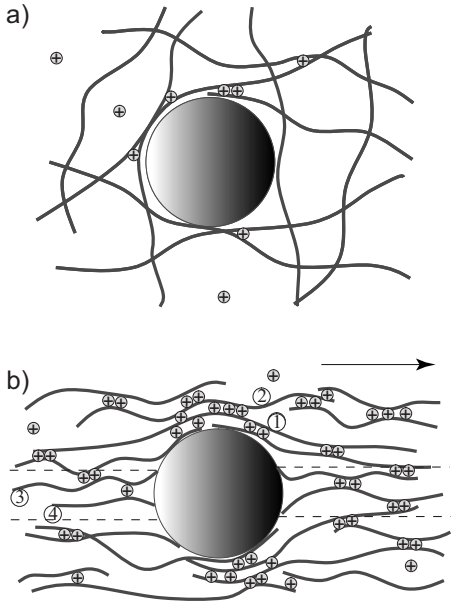

FIG. 9. Illustrations of beads embedded in isotropic (a) and nematic (b) actin networks. The curved lines are actin filaments. "+"s, each enclosed by a circle, represent Mg^{2+} ions. (a) A micron-sized bead embedded in an isotropic actin network. The mesh size in this condition is $\xi=0.3c^{-0.5}=0.3$ μm, where $c=1$ mg/ml. The Mg^{2+} ions only occasionally associate two filaments over their parallel parts or at their junctions. (b) A micron-sized bead embedded in a nematic actin network. The average spacing of two neighboring filaments estimated using a hexagonal lattice model is $d=0.17c^{-0.5}=0.085$ μm, where $c=4$ mg/ml. The Mg^{2+} ions more frequently associate neighboring filaments in the nematic phase, since they are mostly parallel to each other.

filament in an entangled network as diffusing in a virtual tube constructed by its neighboring filaments. Consequently, the transverse diffusion of the filament is significantly suppressed, whereas its longitudinal diffusion is mostly unhindered. When the network becomes nematic, we propose that the motion of a single filament can still be modeled as moving in a tube, although the tube is dilated to a certain extent compared with the isotropic phase due to the alignment of filaments [45]. Since the transverse diffusion of the filaments is suppressed, the filaments tangential to the bead [e.g., filaments No. 1 and No. 2 in Fig. 9(b)] experience more restriction in transverse motion. Consequently, they can hardly vacate room for the bead to diffuse. The filaments pushing the bead with their ends [e.g., filaments No. 3 and No. 4 in Fig. 9(b)], however, can more easily diffuse away longitudinally, hence leaving more room for the beads to diffuse. Consequently, the beads diffuse more along the alignment of actin filaments.

The elasticity of noncrosslinked actin network in the linear regime is mostly attributed to bending of filaments (enthalpic elasticity) and longitudinal extension or compression of filaments (entropic elasticity) [47]. In nematic *F*-actin solutions, the bead is embedded in a local arrangement of filaments as illustrated in Fig. 9(b). The filaments contacting the bead tangentially (e.g., No. 1 and No. 2) push the bead in the direction normal to the filament axis via bending of their own contours. Since they are generally aligned while entangled with one another, they can work cooperatively and the elasticity sensed by the tracer bead in the perpendicular direction is therefore strong. The filaments making contact with their ends to the bead (e.g., No. 3 and No. 4) push or pull the bead by extending or compressing their contours. Because these filaments are not anchored, they can readily slide against each other, and hence provide less elastic support. Thus, the elasticity in the parallel direction is weaker than that in the perpendicular direction.

B. Dependence of shear moduli on actin concentration for nematic *F*-actin solutions

Dependence of shear moduli on actin concentration for isotropic solutions has been measured by several research groups [11–14,43]. As far as we know, the work reported here is the first attempt to measure the shear moduli of *F*-actin solutions in the nematic phase using the VPT microrheology. In the isotropic phase (with actin concentration below 2 mg/ml), we found that $G'_{\perp}$ is equal to $G'_{\parallel}$, showing isotropic viscoelasticity (Fig. 7). When the system enters the nematic phase with increased actin concentration, $G'_{\perp}$ becomes larger and increases more steeply than $G'_{\parallel}$. $G'_{\perp}$ scales with actin concentration as $G'_{\perp}\sim c^{1.38\pm0.15}$, whereas $G'_{\parallel}$ depends more weakly on actin concentration and scales as $G'_{\parallel}\sim c^{0.54\pm0.13}$. The ratio of $G'_{\perp}$ to $G'_{\parallel}$ grows from 1 at 1 mg/ml actin concentration to about 4 at 6 mg/ml. This is in the same order of magnitude as reported by Martinoty *et al.* [25] for nematic elastomers, which is a different type of material. The $G'_{\perp}/G'_{\parallel}$ ratio of nematic elastomers is about 1.6 at the transition point.

$G'_{\perp}$ in the nematic phase scales very similarly to the plateau modulus G' measured in the isotropic phase. The bulk rheology measurement by Hinner *et al.* [44] yields G' as a function of actin concentration for isotropic *F*-actin solutions, following $G'\sim c^{1.4}$. Slightly different in exponent, the diffusing wave spectroscopy microrheology of Xu *et al.* [14] gives $G'\sim c^{1.2}$ and the VPT microrheology of Gardel *et al.* [42] gives $G'\sim c^{1.8}$ for isotropic *F*-actin solutions. The theoretical form of plateau modulus of isotropic entangled semiflexible polymer networks has been obtained by Isambert and Maggs [48] and Morse [46] as

$$G' \sim \rho k_B T/l_e \sim c^{7/5}/l_p^{1/5}, \tag{11}$$

where ρ is the number density of the polymers, c is the mass concentration in mg/ml, l_p is the persistent length, and l_e is the entanglement length. $l_e\sim\xi^{4/5}/l_p^{1/5}$, with ξ being the mesh size and $\xi=0.3c^{-1/2}$. If $G'_{\perp}$ in the nematic phase follows the same scaling behavior as G' in the isotropic phase, we would expect that the rationale deriving Eq. (11) still holds, which means that entanglement still exists in the nematic phase and l_e scales with concentration with the same exponent. As the filaments align in the nematic phase, the mesh can be understood as elongated along the nematic director and the segments constructing the mesh become longer. Since the mesh in the nematic phase becomes asymmetric along and perpendicular to the alignment, it may require two parameters to describe the mesh size, i.e., $\xi_{\parallel}$ and $\xi_{\perp}$ (dimensions along and perpendicular to the alignment) with $\xi_{\parallel}>\xi_{\perp}$. The perpen-

dicular elasticity sensed by the probe beads is still caused by an entangled filament mesh. Thus, $G'_{\perp}$ remains inversely proportional to l_e [Eq. (11)], which is then related to $\xi_{\parallel}$ and $\xi_{\perp}$. Although the ratio of $\xi_{\parallel}$ to $\xi_{\perp}$ depends on the nematic order parameter, both $\xi_{\parallel}$ and $\xi_{\perp}$ vary with actin concentration similarly to ξ in the isotropic phase. Hence, we expect a similar scaling relation of $G'_{\perp}$ with actin concentration. The physical picture put forth here reinforces the concept of entanglement in the nematic phase. This concept has recently been introduced based on the experimental finding that the order parameter of nematic *F*-actin solutions is significantly smaller than 1 [8].

$G'_{\parallel}$ in the nematic phase scales approximately as $G'_{\parallel} \sim c^{0.5}$. If the $G'_{\parallel}$ is mostly due to the pushing of the filaments by their ends (filaments No. 3 and No. 4 in Fig. 9(b)), one would expect $G'_{\parallel}$ to be proportional to c and the scaling exponent to be 1. One explanation to this 0.5 exponent is that due to the increase of actin concentration the filaments become more and more aligned, enhancing the sliding motion of filaments with respect to each other. This effect reduces the increase of elastic support due to the increase of the number of pushing filaments. Therefore, $G'_{\parallel}$ is smaller than being proportional to c. An alternative explanation is that the cross section of the virtual cylinder [between the two dashed lines in Fig. 9(b)] accommodating the filaments contributing to the elastic support in the parallel direction shrinks due to the increased osmotic pressure on the cylinder with the increased actin concentration. The elastic support in the parallel direction should be proportional to the cross-section area times actin concentration. With a decreasing cross-sectional area, consequently, we see the scaling behavior of $G'_{\parallel}$ on actin concentration with an exponent smaller than 1.

C. Viscoelasticity of *F*-actin solutions altered by Mg^{2+} concentration

In the isotropic phase, the storage shear moduli increase with $[Mg^{2+}]$ up to 6 mM and then saturate [Fig. 8(a)]. There are also 50 mM K^+ and 0.2 mM Ca^{2+} in the actin solution, ensuring predominant actin polymerization under all Mg^{2+} concentrations. The dependence of $[Mg^{2+}]$ can be interpreted by the temporary association between segments of two neighboring filaments especially when they are parallel. The effect has been detected as the slowdown of *F*-actin diffusion in the nematic phase with increasing $[Mg^{2+}]$ [32]. These temporary associations are likely caused by the counterion mediated attraction between neighboring filaments at their junctions facilitated by the condensed counterions. These temporary associations act similar to weak crosslinkers, which increase the elasticity of the network [Fig. 9(b)].

In the nematic phase, both $G'_{\parallel}$ and $G'_{\perp}$ increase with the increase in $[Mg^{2+}]$ over a wider range [Fig. 8(b)]. The temporary associations facilitated by condensed Mg^{2+} ions are more favorable in the nematic phase than in the isotropic phase, since the filaments are mostly aligned in the nematic phase. These associations cause parallel filaments like those illustrated on the top and bottom of the bead in Fig. 9(b) (e.g., filaments No. 1 and No. 2) to bend more collectively, thus increasing $G'_{\perp}$. However, these associations do not contribute strongly to the energy dissipation of transverse motion of the bead. Hence, $G''_{\perp}$ is not significantly affected by $[Mg^{2+}]$. In the parallel direction, the associations help immobilize the relative sliding between filaments, causing the filaments on left and right of the bead [e.g., filaments No. 3 and No. 4 in Fig. 9(b)] to provide more elastic support, and thereby increasing $G'_{\parallel}$. We have shown previously that Mg^{2+} causes a progressive slowdown of the longitudinal diffusion of filaments and increases in the friction between neighboring filaments [32]. It is intriguing to note that $G''_{\parallel}$ increases with $[Mg^{2+}]$ only moderately. We conclude that the beads probe more directly the dissipation of the neighboring network, whereas the single filament motion is affected by the interaction with its neighboring filament more sensitively.

V. SUMMARY

We apply both VPT and LDPT microrheology methods to probe viscoelastic properties of *F*-actin across the isotropic-nematic phase transition region. The two methods give consistent results for G' and G''. For isotropic *F*-actin solutions, the viscoelastic moduli are isotropic; in the nematic phase, *F*-actin solutions are more viscoelastic in the direction perpendicular to the nematic director. At low actin concentrations, $G'_{\parallel}$ and $G'_{\perp}$ are equal. As the actin concentration increases above the onset concentration of isotropic-nematic transition, $G'_{\parallel}$ and $G'_{\perp}$ grow apart from each other, with $G'_{\perp}$ larger than $G'_{\parallel}$. $G'_{\parallel}$ scales with actin concentration weakly as $G'_{\parallel} \sim c^{0.54}$. $G'_{\perp}$ follows a scaling relation of $G'_{\perp} \sim c^{1.38}$, nearly the same as the plateau modulus in the isotropic phase. In the nematic phase, parallel filaments bend cooperatively due to the remaining entanglement, contributing to stronger viscoelasticity in response to transverse deformation, whereas the filaments can readily slide against each other along the nematic director, thus leading to reduced viscoelasticity along the direction of alignment.

Furthermore, we studied and compared the effect of $[Mg^{2+}]$ on G' and G'' for isotropic and nematic *F*-actin solutions. For the isotropic phase, G' increases with $[Mg^{2+}]$ in a limited range and then plateaus. For the nematic phase, both $G'_{\parallel}$ and $G'_{\perp}$ increase progressively with $[Mg^{2+}]$ in the whole range below the *F*-actin bundling threshold concentration, which is about 16 mM. The increase of G's is attributed to the temporary association between neighboring filaments induced by the condensed Mg^{2+} ions. The increase of G' is more pronounced in the nematic phase since the Mg^{2+} mediated attraction is more tangible between parallel filaments. In both isotropic and nematic phases, G'' only weakly depends on $[Mg^{2+}]$.

In conclusion, the study of microrheological properties of *F*-actin solutions using particle tracking methods across the isotropic-nematic phase transition under various Mg^{2+} concentrations unites the pertinent effects of alignment and electrostatic interaction between the protein filaments. The results of this study provide a valuable example that the microrheological approach leads to useful insights on the viscoelastic properties of a wide range of biological and synthetic polymeric materials.

ACKNOWLEDGMENTS

We thank Dr. Karim Addas for his earlier work on setting up the laser trap used in this study and Professor Christoph F. Schmidt for an insightful discussion on data interpretation. This work was supported in part by the Petroleum Research Fund (Grant No. PRF 42835-AC7), administered by the American Chemical Society.

[1] A. R. Bausch and K. Kroy, Nat. Phys. **2**, 231 (2006).
[2] H. Isambert, P. Vernier, A. Maggs, A. Fattoum, R. Kassab, D. Pantaloni, and M. F. Carlier, J. Biol. Chem. **270**, 11437 (1995).
[3] F. Gittes, B. Mickey, J. Nettlenton, and J. Howard, J. Cell Biol. **120**, 923 (1993).
[4] K. C. Holmes, D. Popp, W. Gebhard, and W. Kabsch, Nature (London) **347**, 44 (1990).
[5] C. Coppin and P. Leavis, Biophys. J. **63**, 794 (1992).
[6] R. Furakawa, R. Kundra, and M. Fechheimer, Biochemistry **32**, 12346 (1993).
[7] J. Viamontes, P. W. Oakes, and J. X. Tang, Phys. Rev. Lett. **97**, 118103 (2006).
[8] J. Viamontes, S. Narayanan, A. R. Sandy, and J. X. Tang, Phys. Rev. E **73**, 061901 (2006).
[9] T. G. Mason and D. A. Weitz, Phys. Rev. Lett. **74**, 1250 (1995).
[10] T. G. Mason, K. Ganesan, J. H. van Zanten, D. Wirtz, and S. C. Kuo, Phys. Rev. Lett. **79**, 3282 (1997).
[11] B. Schnurr, F. Gittes, F. C. MacKintosh, and C. F. Schmidt, Macromolecules **30**, 7781 (1997).
[12] F. Gittes, B. Schnurr, P. D. Olmsted, F. C. MacKintosh, and C. F. Schmidt, Phys. Rev. Lett. **79**, 3286 (1997).
[13] A. Palmer, J. Xu, and D. Wirtz, Rheol. Acta **37**, 97 (1998).
[14] J. Xu, A. Palmer, and D. Wirtz, Macromolecules **31**, 6486 (1998).
[15] T. G. Mason, Rheol. Acta **39**, 371 (2000).
[16] A. J. Levine and T. C. Lubensky, Phys. Rev. Lett. **85**, 1774 (2000).
[17] K. M. Addas, C. F. Schmidt, and J. X. Tang, Phys. Rev. E **70**, 021503 (2004).
[18] R. R. Brau, J. M. Ferrer, H. Lee, C. E. Castro, B. K. Tam, P. B. Tarsa, P. Matsudaira, M. C. Boyce, R. D. Kamm, and M. J. Lang, J. Opt. A, Pure Appl. Opt. **9**, S103 (2007).
[19] T. Asada, H. Muramatsu, R. Watanabe, and S. Onogi, Macromolecules **13**, 867 (1980).
[20] K. F. Wissbrun, J. Rheol. **25**, 619 (1981).
[21] G. C. Berry, Mol. Cryst. Liq. Cryst. **165**, 333 (1988).
[22] W. R. Burghardt and G. G. Fuller, Macromolecules **24**, 2546 (1991).
[23] J.-L. Gallani, L. Hilliou, P. Martinoty, F. Doublet, and M. Mauza, J. Phys. II **6**, 443 (1996).
[24] P. Stein, N. Aβfalg, H. Finkelmann, and P. Martinot, Eur. Phys. J. E **4** 255 (2001).
[25] P. Martinoty, P. Stein, H. Finkelmann, H. Pleiner, and H. Brand, Eur. Phys. J. E **14**, 311 (2004).
[26] O. Stenull and T. Lubensky, Eur. Phys. J. E **14**, 333 (2004).
[27] F. Oosawa, *Polyelectrolytes* (Marcel Dekker, New York, 1971).
[28] G. S. Manning, J. Chem. Phys. **51**, 924 (1969).
[29] Q. Wen and J. X. Tang, Phys. Rev. Lett. **97**, 048101 (2006).
[30] J. X. Tang and P. A. Janmey, J. Biol. Chem. **271**, 8556 (1996).
[31] T. E. Angelini, H. Liang, W. Wriggers, and G. C. L. Wong, Proc. Natl. Acad. Sci. U.S.A. **100**, 8634 (2003).
[32] J. He, J. Viamontes, and J. X. Tang, Phys. Rev. Lett. **99**, 068103 (2007).
[33] J. Xu, D. Wirtz, and T. D. Pollard, J. Biol. Chem. **273**, 9570 (1998).
[34] M. L. Gardel, J. H. Shin, F. C. MacKintosh, L. Mahadevan, P. Matsudaira, and D. A. Weitz, Science **304**, 1301 (2004).
[35] J. D. Pardee and J. A. Spudich, Methods Cell Biol. **24**, 271 (1982).
[36] R. Oldenbourg and G. Mei, J. Microsc. **180**, 140 (1995).
[37] R. Oldenbourg, E. D. Salmon, and P. T. Tran, Biophys. J. **74**, 645 (1998).
[38] L. D. Landau, E. M. Lifshitz, and L. P. Pitaevskii, *Statistical Physics* (Pergamon Press, Oxford, England, 1980).
[39] T. C. Lubensky, D. Pettey, N. Currier, and H. Stark, Phys. Rev. E **57**, 610 (1998).
[40] R. S. Pillai, M. Oh-e, H. Yokoyama, G. J. Brakenhoff, and M. Müller, Opt. Express **14** 12976 (2006).
[41] I. I. Smalyukh, A. V. Kachynski, A. N. Kuzmin, and P. N. Prasad, Proc. Natl. Acad. Sci. U.S.A. **103**, 18048 (2006).
[42] M. L. Gardel, M. T. Valentine, J. C. Crocker, A. R. Bausch, and D. A. Weitz, Phys. Rev. Lett. **91**, 158302 (2003).
[43] T. G. Mason, T. Gisler, K. Kroy, E. Frey, and D. A. Weitz, J. Rheol. **44** (4), 917 (2000).
[44] B. Hinner, M. Tempel, E. Sackmann, K. Kroy, and E. Frey, Phys. Rev. Lett. **81**, 2614 (1998).
[45] M. Doi and S. F. Edwards, *The Theory of Polymer Dynamics* (Oxford University Press, Oxford, 1986).
[46] D. C. Morse, Phys. Rev. E **63**, 031502 (2001).
[47] K. Kroy and E. Frey, Phys. Rev. Lett. **77**, 306 (1996).
[48] H. Isambert and A. C. Maggs, Macromolecules **29**, 1036 (1996).